Journal of Materials Science: Materials in Electronics (2020) 31:6017–6026
https://doi.org/10.1007/s10854-020-03153-9

Amperometric detection of hydrogen peroxide and its density functional theory for adsorption on Ag/TiO_2 nanohybrid

Su Pei Lim[1,2] · M. M. Shahid[3] · Perumal Rameshkumar[4] · Nay Ming Huang[1,2] · Liming Che[1,2]

Received: 29 November 2019 / Accepted: 20 February 2020 / Published online: 2 March 2020

Abstract

Silver/titania (Ag/TiO_2) nanocomposites, synthesized through a simple one-step chemical reduction method, are used for electrochemical sensing of hydrogen peroxide (H_2O_2). The images of transmission electron microscopic (TEM) demonstrate a well dispersion of Ag nanoparticles (NPs) with a particle size range of approximately 3 nm on the TiO_2 surface, which makes the sensor based on Ag/TiO_2 exhibit an excellent performance toward H_2O_2. The AgNPs presented in the nanocomposite exhibit electrocatalytic reduction of H_2O_2 and the limit of detection (LOD) is found to be 1.23 µM. Density functional theory (DFT) calculation studies reveal that H_2O_2 could be easily adsorbed onto Ag rather than TiO_2 surface of Ag/TiO_2 via a partial electron transfer from Ag to H_2O_2. The nanocomposite-modified electrode has also excellent selectivity toward the detection of H_2O_2 over the interferents even when the interferents have a 100 times higher concentration than H_2O_2.

1 Introduction

The sensitivity and accurate determination of small quantities of H_2O_2 is utmost important because of its wide use in food industry, pharmaceutical, environmental analysis, biomedical fields, and enzymatic reactions [1]. Accidental ingestion of H_2O_2 will lead to diseases such as asthma, cancer, and diabetes and even will cause death for high consumption of H_2O_2. With the increasing number of important applications of H_2O_2, different methods have been utilized toward the detection of H_2O_2, such as chemiluminescence [2], fluorescence [3], and spectrophotometry [4]. Yet, these techniques are usually not easy to use, time consuming, and sometimes costly. Since H_2O_2 itself is an electroactive material, constructing a competent electrochemical sensor has gained much interest among researchers due to its ease of the operation, low cost, and high selectivity [5, 6], certainly depending on the material used for the sensor.

In recent year, metal oxide materials emerged as promising materials for sensing applications. A large variety of oxide compounds can be formed from metal elements that can adopt a vast number of structural geometries with an electronic structure that can exhibit metallic, semiconductor, or insulator character. Due to the widespread structural, physical properties, chemical properties, and functionalities, metal oxides had stand out as one of the most common, diverse, and richest classes of materials [7]. Metal oxides proved to be very promising for a variety of technological applications due to their unique and tunable properties such as optical, magnetic, electrical, catalytic, photochemical properties [8–10]. The metal oxides, such as modified zinc oxide (ZnO) [11], titanium oxide, (TiO_2) [12, 13] tin oxide (SnO_2) [14], zirconium oxide (ZrO_2) [15], manganese dioxide (MnO_2) [16], copper(II) oxide (CuO) [17], and cerium oxide (CeO_2) [18, 19], have been widely investigated as sensing material. So far, TiO_2 has attracted much interest owing to its low cost, abundance,

Electronic supplementary material The online version of this article (https://doi.org/10.1007/s10854-020-03153-9) contains supplementary material, which is available to authorized users.

✉ Su Pei Lim
splim@xmu.edu.my

✉ Perumal Rameshkumar
rameshkumar.p@klu.ac.in

✉ Liming Che
lmc@xmu.edu.cn

1 School of Energy and Chemical Engineering, Xiamen University Malaysia, Jalan Sunsuria, Bandar Sunsuria, 43900 Sepang, Selangor Darul Ehsan, Malaysia

2 College of Chemistry and Chemical Engineering, Xiamen University, Xiamen 361005, China

3 Micro-Nano System Centre, School of Information Science & Technology, Fudan University, Shanghai 200433, China

4 Department of Chemistry, Kalasalingam Academy of Research and Education, Krishnankoil, Tamil Nadu 626 126, India

non-toxicity, safety, high specific surface area, and biocompatibility [20, 21].

Nowadays, non-enzymatic electrochemical sensors have attracted much attention from the researchers to avoid the disadvantage of the enzyme-based biosensors [22]. Therefore, a plenty of studies have been carried out to improve the non-enzymatic electrochemical sensors with low detection limit. With the development of nanotechnology, many nanomaterials have been applied in the field of enzyme-free sensors due to their excellent conductivity, extraordinary electrocatalytic, large specific surface areas, and biocompatibilities. Among these, metal nanoparticles, such as gold (Au) [23, 24], copper (Cu) [25, 26] platinum (Pt) [27, 28], and palladium (Pd) [29, 30] were employed to construct H_2O_2 sensor. Silver nanoparticles (AgNPs) have aroused growing interest in recent years, because they not only have common characteristics of noble metals nanoparticles but also have unique properties of outstanding conductivity, electroactivity, low toxicity, and low cost [12–14, 31, 32]. However, the aggregation of AgNPs prohibits extensive applications because of the poor stability and reproducibility, and thus highly dispersed AgNPs are very important in fabricating a sensor [33]. In this regard, the supported system had a major influence on fabricating highly dispersed AgNPs for efficient sensor application. Recently, TiO_2 has gained increasing attraction as an ideal material for the supported system to fabricate sensors owing to its special characteristics, especially the property of the strong metal-support interactions (SMSI). The TiO_2 particles will provide large surface area and strong interaction between Ti and Ag for the stable deposition of AgNPs and the AgNPs facilitate an efficient electron transfer process during the electrocatalytic reduction of H_2O_2, thus improving the sensing performance.

In this study, we successfully developed a facile, one-step chemical reduction method to prepare homogeneously distributed Ag nanoparticles deposited on TiO_2 without addition of any stabilizer or surfactant. The Ag/TiO_2 nanocomposite-modified electrode showed better catalytic performance compared to that of a bare TiO_2. The effect of the Ag content on the catalytic performance was also investigated. The detection of H_2O_2 was studied using the amperometric *i–t* curve technique and limit of detection was found to be 1.23 µM with signal-to-noise (S/N) ratio around 3. Furthermore, the nanocomposite-modified electrode demonstrated excellent selectivity toward the detection of H_2O_2 in the presence of 100 times higher concentration of other important interferents.

2 Experimental methods

2.1 Materials

Titanium dioxide (P25), silver nitrate ($AgNO_3$), and sodium borohydride ($NaBH_4$) were purchased from Merck and used them as received. H_2O_2 was obtained from Sigma-Aldrich. All chemicals used were of analytical reagent grade and doubly distilled water was used for all the experiments.

2.2 Synthesis of Ag/TiO_2 nanocomposite

Firstly, 500 mg of P25 was added to different amounts of aqueous $AgNO_3$ (5, 10, 20, and 40 wt%). Each mixture was vigorously stirred for half hour at room temperature. The reduction of Ag^+ was initiated when $NaBH_4$ was added and the solution changed to greenish yellow. The mixture was then stirred for another half hour. The greenish yellow solution was centrifuged and washed repeatedly using distilled water and ethanol. Finally, the solution was then dried in an oven at 60 °C to obtain the Ag/TiO_2 nanocomposite. The nanocomposite with 20 wt% of Ag was used for all the characterizations and detection of H_2O_2 unless otherwise stated.

2.3 Fabrication of Ag/TiO_2-modified electrode and electrochemical measurements

The Ag/TiO_2 nanocomposite was prepared following the previous method [34] with some modifications. The detailed method is described in supplementary information. Prior to modification, the glassy carbon electrode (GCE) was carefully polished with alumina slurry suspension (5 µM) on the micro-cloth polishing pad followed by ultrasonically cleaned with distilled water and ethanol for 2 min. Next, 5µL of the nanocomposite solution (1 mg/mL) was dropped onto a GCE surface, allowed to dry at room temperature (25 °C) for 1 h. The prepared Ag/TiO_2-modified GCE was used as a working electrode for further investigation.

2.4 Characterization techniques

Transmission electron microscopy (TEM) images were captured using JEOL JEM-2100 F high-resolution transmission electron microscope (HRTEM) operated at 200 kV. The optical absorption properties in the spectral region of 200–800 nm were examined using a Thermo Scientific Evolution 300 UV–Vis absorption spectrophotometer. Raman spectra were recorded with Renishaw inVia 2000 system with an argon ion laser emitting at 532 nm. The crystalline phase of the samples was studied via X-ray diffraction (XRD; D5000, Siemens), using copper Kα radiation ($\lambda = 1.5418$ Å) at a scan rate of $0.02^\circ\ s^{-1}$. All the electrochemical studies were carried out using a VersaSTAT-4 electrochemical analyzer (Princeton Applied Research, USA) with a conventional three-electrode system. The fabricated GCE was used as a working electrode, silver/silver chloride (Ag/AgCl) as reference electrodes, and Platinum (Pt) as counter electrode. X-ray photoelectron spectroscopy (XPS) measurements were taken by synchrotron radiation

from beam line no. 3.2 at the Synchrotron Light Research Institute, Thailand.

2.5 Density functional theory (DFT) calculation

All DFT calculations, i.e., geometry optimization, were performed using the DMol^3 program package [35] (Materials Studio 8.0, BIOVIA, San Diego, USA). The method proposed by Tkatchenko and Scheffler (TS) was employed to correct the calculations for missing van der Waals interaction [36]. Generalized gradient approximation (GGA) with the Perdew–Burke–Ernzerhof (PBE) functional was employed to account for the exchange–correlation interaction [37]. Spin-polarized calculations were carried out with double numerical plus polarization (DNP) basis set. All electrons were included in the calculations. The Brillouin zone was sampled only at Gamma-point. The orbital occupancy thermal smearing was set to 0.005 Ha. The convergence criteria for the maximum energy change, the maximum force, and the maximum displacement were set to 10^{-5} Ha, 0.002 Ha·Å^{-1}, and 0.005 Å, respectively.

3 Results and discussion

3.1 Morphological studies and optical properties of Ag/TiO_2 nanocomposite

The physical appearance of Ag/TiO_2 with is shown in Fig. 1a. The morphology and structure of the Ag/TiO_2 nanocomposite was characterized with TEM. The analysis of TEM images revealed that the TiO_2 particles have a size range of 20–25 nm (Fig. 1b, c). AgNPs had a diameter of approximately 3 nm and are well dispersed and deposited on the surface of TiO_2 (Fig. 1c). Figure 1d indicates the UV–Vis absorption spectra of the TiO_2 particles and Ag/TiO_2 nanocomposite. TiO_2 did not have any absorbance in the visible region because of the wide band gap energy (~ 3.2 eV). The deposition of AgNPs on the TiO_2 surface significantly influenced the absorption in the visible regions of 450–600 nm, which was due to the surface plasmon resonance (SPR) band of AgNPs. It can be seen that the absorption edge also shifts toward visible region for Ag/TiO_2 sample due to the influences of AgNPs on

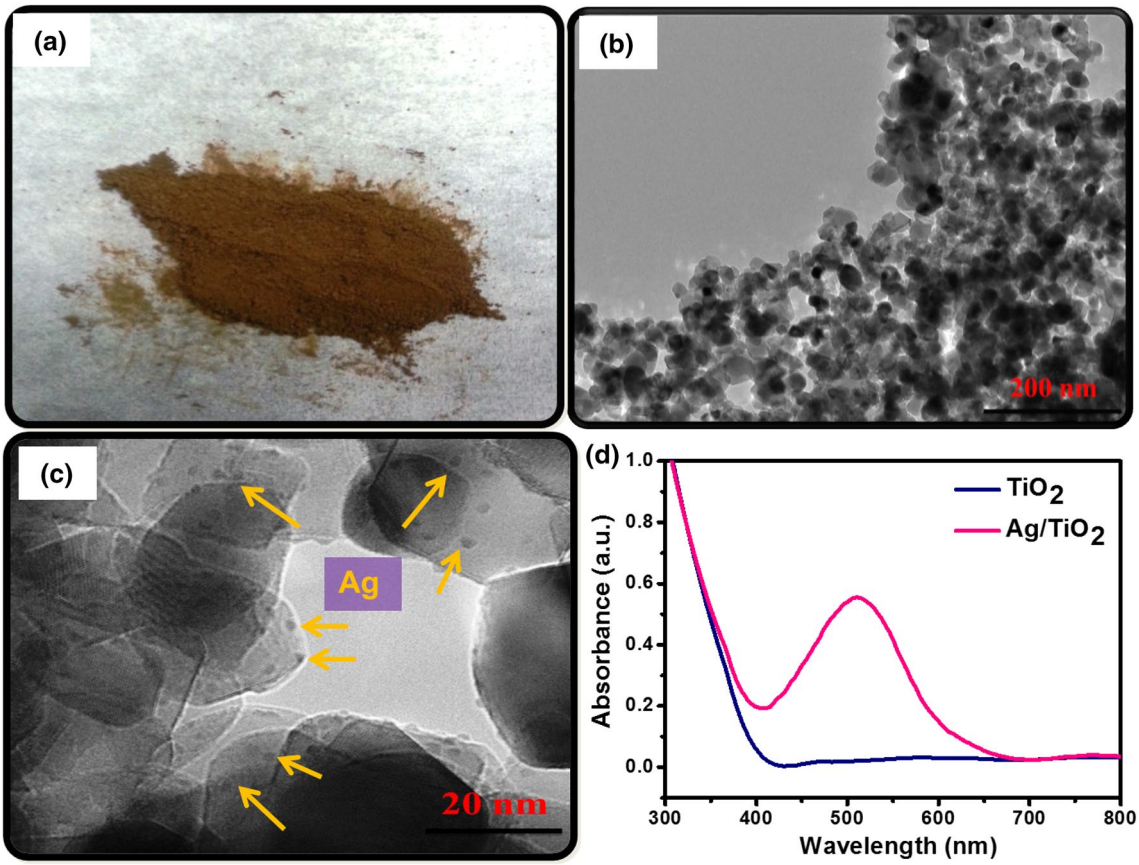

Fig. 1 **a** Physical appearance of the Ag/TiO_2 nanocomposite. **b**, **c** TEM images of Ag/TiO_2 nanocomposite at different magnifications. **d** Absorption spectra of TiO_2 particles and Ag/TiO_2 nanocomposite

the absorption properties of TiO_2 based on the figure that compared to pure TiO_2.

3.2 XPS and Raman analyses of Ag/TiO_2 nanocomposite

In order to understand the chemical components of the samples, the Ag/TiO_2 nanocomposite XPS spectra were analyzed and are demonstrated in Fig. 2. The scanned surface spectra illustrate the chemical composition of elemental Ti, O, and Ag in the Ag/TiO_2 nanocomposite. The binding energies of Ag $3d_{5/2}$ and Ag $3d_{3/2}$ levels are found to be 368.5 and 374.5 eV in Fig. 2a, respectively, with a peak separation of 6 eV attributing to the formation of the metallic silver [38]. Ti 2p spectra for Ag/TiO_2 are observed at 454.2 and 459.8 eV corresponding to the binding energies of the Ti $2p_{3/2}$ and Ti2 $p_{1/2}$ core levels in the presence of the Ti(IV) state (Fig. 2b). The X-ray diffraction patterns indicated that TiO_2 and Ag/TiO_2 were composed of mixed anatase and rutile phases (Figure S1), which closely matches the reference patterns of JCPDS card No. 83-2243 and 21-127, respectively. The diffraction peaks observed at the 2θ values of 25.35°, 38.78°, 47.15°, and 75.4° corresponded to the anatase phase of TiO_2 and were assigned to the (101), (004), (200), and (215) crystallographic planes, respectively. In contrast, the peaks at the 2θ values of 54.8° and 63.8° agreed well with the rutile phase of TiO_2 and were are assigned to the (220) and (002) crystallographic planes, respectively. From the XRD analysis, the crystallographic peaks due to Ag overlapped with those for the rutile phase of TiO_2. Hence, the peaks were indistinguishable in Ag@TiO_2. Raman spectroscopy for TiO_2 and Ag/TiO_2 nanocomposite was also collected in order to evaluate the phase identification of the nanocomposites (Fig. 3). The bands at 153.35, 198.74, 396.32, 521.19, and 637.41 cm^{-1} are characteristic of anatase phase TiO_2. However, no signal related to AgNPs was identified perhaps because of the relatively low concentration of Ag loaded onto TiO_2 and its weak Raman scattering.

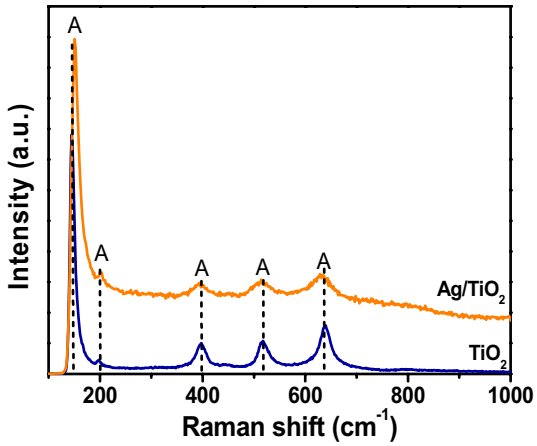

Fig. 3 Raman spectra of TiO_2 and Ag/TiO_2 nanocomposites

3.3 EIS study

The interfacial electron transfer properties and impedance changes of the surface-modified electrodes were studied by the electrochemical impedance spectroscopy (EIS) technique. The 1 mM $[Fe(CN)_6]^{3-/4-}$ in 0.1 M KCl was applied as a redox analyte to study the conducting behavior of the Ag/TiO_2 nanocomposite-modified electrode. Normally, the diameter of the semicircle at higher frequencies in the Nyquist diagram is related to the electron transfer resistance (R_{ct}) [39]. As shown in Fig. 4a, the Ag/TiO_2-modified electrode shows a smallest Rct value (~ 54,569 Ω) compared to bare GCE (~ 198,628 Ω) and TiO_2 (~ 67,833 Ω)-modified electrode under given experimental conditions. This indicated that the presence of Ag at the modified electrode efficiently facilitated the electron transfer process. Furthermore, bode phase of the modified electrodes was collected in the frequency range of 0.01–1000 Hz that corresponds to the charge-transfer resistance of the modified electrodes. The shifting of peaks toward the low-frequency region for the TiO_2 and Ag/TiO_2 nanocomposite indicates the efficient electron transfer

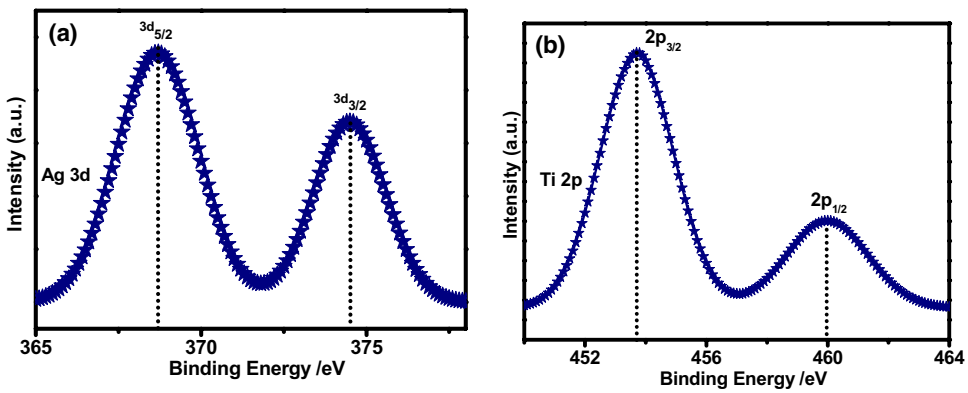

Fig. 2 XPS spectra of Ag/TiO_2 and the corresponding **a** Ag 3d and **b** Ti 2p core-level spectra

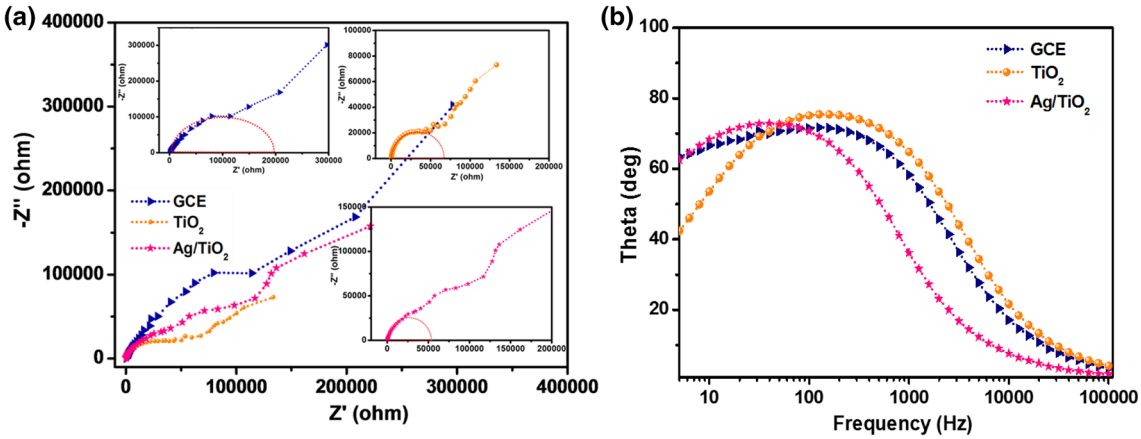

Fig. 4 **a** Nyquist plots and **b** Bode angle phase plots for GCE, TiO_2, and Ag/TiO_2 nanocomposite (20 wt% of Ag)

behavior of the nanocomposites as compared to the bare GCE (Fig. 4b).

3.4 Electrocatalytic reduction of H_2O_2

The electrocatalytic behavior of the Ag/TiO_2 nanocomposite toward the reduction of a 1 mM H_2O_2 in 0.1 M PBS (pH 7.2) was investigated with cyclic voltammetry and the results are presented in Fig. 5a. No significant catalytic response peak was observed for the reduction of H_2O_2 at bare GCE and TiO_2-modified electrode. However, a significant catalytic current response was observed at an over potential of − 0.57 V for Ag/TiO_2 nanocomposite-modified electrode toward the reduction of 1 mM H_2O_2. This clearly reveals that excellent electrocatalytic properties of AgNPs for 1 mM H_2O_2 reduction. Hence, the current response corresponding to the reduction of H_2O_2 can be amplified by optimizing Ag content on TiO_2. Optimization of the amount of Ag on TiO_2 is essential for the economic and high-performance perspectives of a sensor. The current response increased with the increasing amount of Ag on TiO_2 and the catalytic peak at − 0.57 V became significant for Ag/TiO_2(20 wt% of Ag) nanocomposite-modified electrode. The TiO_2 particles provide large surface area for the stable deposition of AgNPs and the AgNPs facilitate an efficient electron transfer process during the electrocatalytic reduction of H_2O_2. A further increase in the Ag content eventually led to a decrease in the catalytic current for the reduction of 1 mM H_2O_2.

The cyclic voltammograms were recorded at the Ag/TiO_2(20 wt% Ag) nanocomposite-modified electrode for the reduction of different concentrations of H_2O_2 in 0.1 M PBS (pH 7.2) and the voltammetric curves are displayed in Fig. 5b. It can be seen that no characteristic peak was observed in the absence of H_2O_2. When H_2O_2 was introduced into the PBS, the reduction peak appeared and it increased with respect to the concentration of the H_2O_2, indicating the good electrocatalytic activity of the nanocomposite toward H_2O_2 reduction. It was also observed that the plot of peak current versus concentration of H_2O_2 showed a linear relation (Fig. 5c). The plot of log(current) versus log[H_2O_2] (Figure S2) showed a linear relation with a slope ~ 1, which indicates that the electro-reduction of H_2O_2 at Ag/TiO_2-modified electrode follows the first-order kinetics with respect to the H_2O_2 concentration. The cyclic voltammograms of Ag/TiO_2 nanocomposite-modified electrode were recorded at different scan rates from 10–100 mV/s for the reduction of 1 mM H_2O_2 in 0.1 M PBS and are shown in Figure S3A. A linear relation between the peak currents and square root of scan rates was also obtained (Figure S3B) which indicates that the H_2O_2 reduction at the nanocomposite-modified electrode is controlled by the diffusion process.

3.5 Amperometric detection of H_2O_2

Selective detection of the particular analyte for the common interferent species can be obtained using amperometric (*i–t*) technique tool. The Ag/TiO_2 nanocomposite with 20 wt% Ag was chosen for the sensitive and non-enzymatic determination of H_2O_2 because of the better catalytic performance in CV. Figure 6 displays the amperometric current–time (*i–t*) curve of the Ag/TiO_2 (20 wt% Ag) nanocomposite-modified electrode in continuously stirred N_2-saturated 0.1 M PBS (pH 7.2) for the injection of different concentrations of H_2O_2 at a regular interval of 60 s with applied potential of − 0.5 V. The lower applied potential was used to avoid or decrease the interferences caused by the electroactive species present in the solution [40]. It can be observed that a significant current response was observed and the sensor showed the current response in less than 3 s for each addition of H_2O_2 with a sample interval of 60 s. This indicates that the AgNPs present in the Ag/TiO_2 nanocomposite can enhance the H_2O_2 accessibility and efficiently promote the electron transfer rate

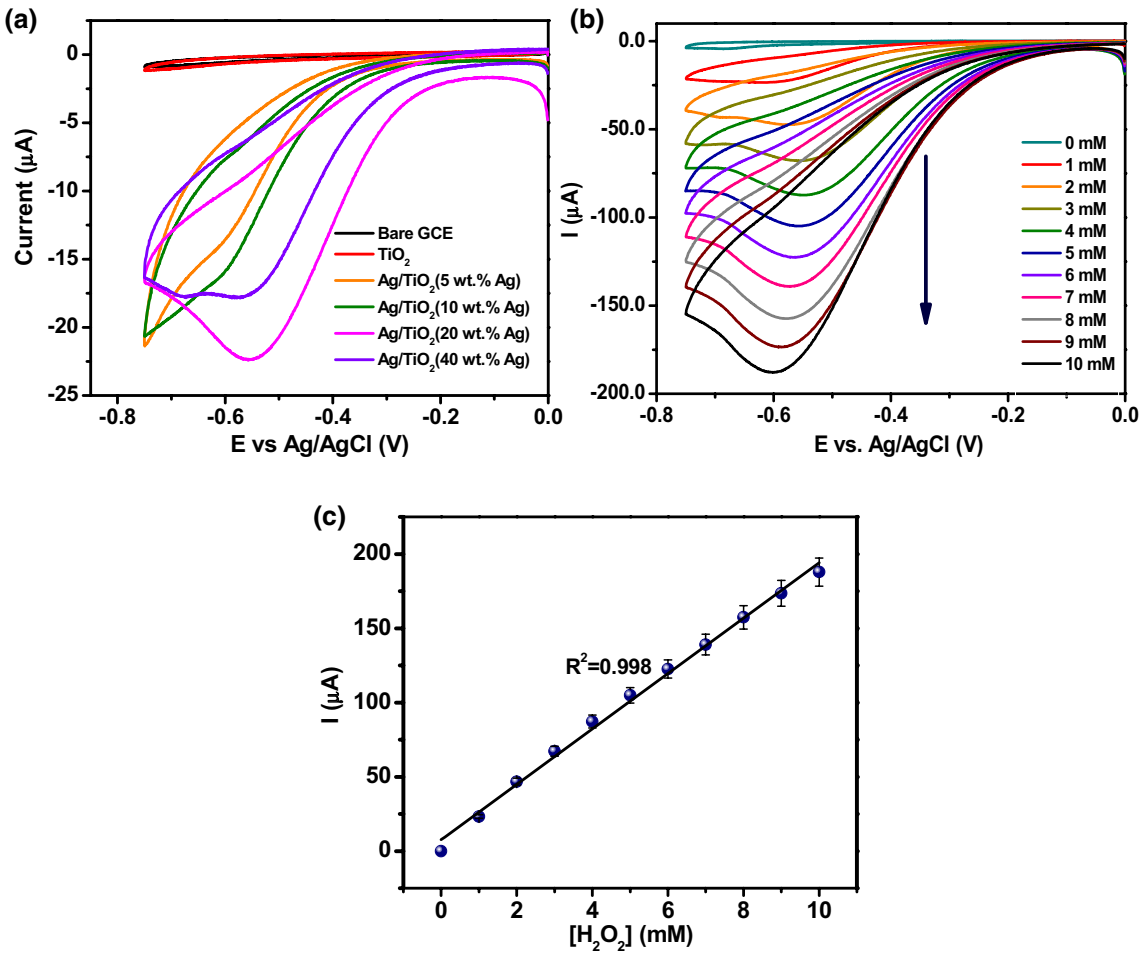

Fig. 5 **a** Cyclic voltammograms obtained for bare GCE, TiO_2, and the Ag/TiO_2 nanocomposite with different wt% of Ag in N_2 saturated 0.1 M PBS (pH 7.2) containing 1 mM H_2O_2 at a scan rate of 50 mV/s. **b** CVs obtained for the Ag/TiO_2 nanocomposite (20 wt% Ag) in N_2 saturated 0.1 M PBS (pH 7.2) containing different concentrations of H_2O_2 at a scan rate of 50 mV/s. **c** Calibration curve of peak current versus concentration of H_2O_2

between the H_2O_2 and electrode surface in PBS. The current response increased for the successive addition of H_2O_2 and multi-linear lines was observed for different concentration ranges. The limit of detection of Ag/TiO_2 (20 wt% of Ag) was found to be 1.23 μM toward the detection of H_2O_2. The comparison of the analytical performance of the present Ag/TiO_2 nanocomposite-modified GCE with previous reports toward detection of H_2O_2 is summarized in Table 1. The present work stands for simple fabrication method for the catalyst and without employing any polymeric binder material or tedious electrode modification process. The proposed modified electrode displayed a satisfactory performance in terms of the detection limit and good selectivity.

3.6 Interference study

Investigation on the selectivity of the Ag/TiO_2 nanocomposite toward the detection of H_2O_2 was then carried out by injecting various possible physiological interferents in the same homogeneously stirred PBS containing H_2O_2. The current responses of the interferents such as ascorbic acid, dopamine, glucose, KCl, $NaNO_3$, Na_2SO_4, and uric acid were studied by adding in sequence after the few consecutive addition of H_2O_2 (50 μM) in the stirred PBS. However, the added interferents did not indicate any current response even with a 100 times higher concentration than the concentration of H_2O_2 (Fig. 7). Addition of interferents creates disturbance in *i–t* curve signal but they did not lead to a stable and significant current response. After the sudden increase in the current response, a fast decay was detected before they reach the steady state. It was then followed by introduction of H_2O_2 to the same solution again which gave a quick response. Moreover, the presence of higher concentration of the interfering ions did not disturb the current signal of H_2O_2 and almost the same magnitudes of current response were reproduced. The present sensor displayed good selectivity

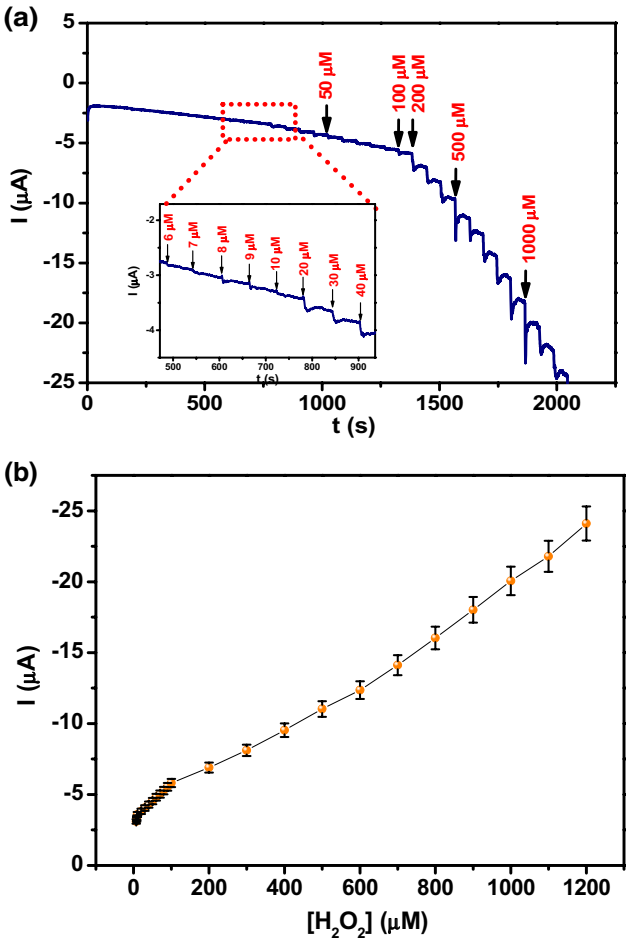

Fig. 6 **a** Amperometric i–t curve obtained at the Ag/TiO_2(20 wt% of Ag) nanocomposite-modified electrode in N_2 saturated 0.1 M PBS (pH 7.2) for the addition of various concentrations of H_2O_2 at a regular internal of 60 s. Applied potential was −0.5 V. **b** Calibration curve of peak current versus concentration of H_2O_2

and sensitivity when compared among the other common interferent species.

3.7 Density functional theory (DFT) calculation

In order to have a deep insight of the adsorption and reduction of H_2O_2 on Ag/TiO_2 nanohybrid, DFT calculation is performed for the nanohybrid model in this work. The calculation followed the procedure reported by Tada et al. with slight modification [44]. As shown in Fig. 8, TiO_2 surface is represented by a $Ti_4O_{10}H_4$ cluster truncated from rutile (110) surface. Hydrogen atom is used to stabilize the dangling bond at peripheral O atom. Even though P25 is mainly composed of anatase (79%), stable and often exposed surface of anatase is not established when compared with the one of rutile. Band structure calculation shows that both surfaces have almost the same electronic property except that the surface of rutile has a slightly smaller band gap. Furthermore, H_2O_2 interacts with Ag nanoparticles rather than TiO_2 surface, and thus the difference in local structure between anatase and rutile does not influence the reduction of H_2O_2 significantly.

As illustrated in Figure S4, Ag nanoparticle is represented by Ag_3 and Ag_4 clusters in this work. On optimizing the structure of Ag cluster on $Ti_4O_{10}H_4$, Ag atoms and the O atom at the top position, which is close to Ag cluster, are optimized, while the other part of $Ti_4O_{10}H_4$ cluster is fixed to the crystalline geometry and the O–H bond length is fixed to 1.0 Å. Figure S5 shows the optimized geometries of Ag clusters on $Ti_4O_{10}H_4$ cluster. The optimized geometry of H_2O_2 is shown in Figure S6. In the case of H_2O_2 adsorption, H_2O_2 is placed initially right above the Ag cluster. H_2O_2 is optimized as well as the Ag atoms and the above-mentioned O atom. Similar to the result of Tada et al. [44], the Ag clusters deposited on $Ti_4O_{10}H_4$ are positively charged. The charges are + 0.714 eV and + 0.767 eV estimated by Mulliken population for Ag_3 and Ag_4, respectively.

The optimized geometry of $H_2O_2/Ag_3/Ti_4O_{10}H_4$ is shown in Fig. 9a. Upon adsorption on $Ag_3/Ti_4O_{10}H_4$, H_2O_2 obtains extra electron from Ag_3 cluster, resulting in the elongation of O–O bond. H_2O_2 is then dissociated into two hydroxyl groups, one of which is adsorbed on Ag_3 cluster with a bond length of 2.246 Å. The hydroxyl groups formed will react further with H^+ to form H_2O. The adsorption energy of H_2O_2 ($E_{ads} = E_{H2O2/Ag4/Ti4O10H4} - E_{H2O2} - E_{Ag4/Ti4O10H4}$) is calculated to be −0.84 eV. The charges estimated by Mulliken population are −0.161 e and −0.156 e for the adsorbed hydroxyl group and free one, respectively. The charge of Ag_3 cluster increases from + 0.714 eV to + 0.926 eV upon the adsorption of H_2O_2, i.e., the loss of electron is less than the one gained by H_2O_2. That means electron is also transferred from $Ti_4O_{10}H_4$ cluster to H_2O_2 via Ag_3 cluster. This is in good agreement with the mechanism presented by Khan et al. [8] Dissociative adsorption of H_2O_2 on $Ag_4/Ti_4O_{10}H_4$ (Fig. 9b) is similar to that on $Ag_3/Ti_4O_{10}H_4$. The adsorption energy of H_2O_2 is −0.76 eV.

To investigate the role of charge in the catalytic activity, H_2O_2 adsorption on charged $Ag_4/Ti_4O_{10}H_4$ cluster was calculated and the optimized geometries are shown in Figure S7. In the case of H_2O_2 adsorption on anionic $Ag_4/Ti_4O_{10}H_4$ cluster (− 1.0 eV), H_2O_2 obtains more electron, i.e., −0.845 eV from $Ag_4/Ti_4O_{10}H_4$. H_2O_2 is dissociated into H_2O and O bonded to Ag_4 cluster. The length of Ag–O bond is 1.988 Å, which is in good agreement with experimental value of 2.0 Å [45]. The adsorption energy of H_2O_2 is calculated to be −2.12 eV. While in the case of H_2O_2 adsorption on cationic $Au_4/Ti_4O_{10}H_4$ cluster (+ 1.0 eV), dissociation of H_2O_2 is not observed due to the lack of free electron. H_2O_2 adsorbed physically to cationic $Au_4/Ti_4O_{10}H_4$ cluster with an adsorption energy of −0.66 eV.

Table 1 A comparison of the reported Ag and Ag/TiO_2 electrochemical sensors with the present nanocomposite for H_2O_2 detection

Sensor electrode	Fabrication method	Analytical technique	LOD (μM)	Interferents studied	Refs
AgNPs/PQ11	Hydrothermal method	Amperometry	33.9	–	[31]
Nanoporous Ag on Titanium surface	Hydrothermal method	Amperometry	210	–	[32]
Ag nanoparticle-TiO_2 nanowire	Hydrothermal followed by UV reduction of Ag	Amperometry	1.70	AA, UA, DA, glucose	[41]
Ag nanoparticle-TiO_2 nanotube	Anodization followed by electrophoretic of Ag	Amperometry	0.085	$Ca(NO_3)_2$, KCl, Na_2SO_4, DA, UA, AA, glucose	[42]
Ag/TiO_2	Biosynthesis using electrochemically active biofilm	DPV	0.83	–	[12]
TiO_2/ rGO/Ag	Anodization followed by immersion and chemi-deposition of Ag	Amperometry	2.2	Glucose	[13]
Ag/ TiO_2/poly(vinyl alcohol) (PVA)	sol–gel process and photochemical reduction of Ag on TiO_2/ PVA	Amperometry	0.11	AA, UA, AP	[43]
Ag/TiO_2 nanocomposite	Chemical Reduction method	Amperometry	1.23	AA, DA, glucose, KCl, $NaNO_3$, Na_2SO_4, UA	Present work

rGO reduced graphene oxide, *DPV* different pulse voltammetry, *AA* ascorbic acid, *UA* Uric acid, *DA* dopamine, *$Ca(NO_3)_2$* calcium nitrate, *KCl* potassium chloride, *Na_2SO_4* sodium sulfate, *$NaNO_3$* sodium nitrate, *AP* acetaminophen.

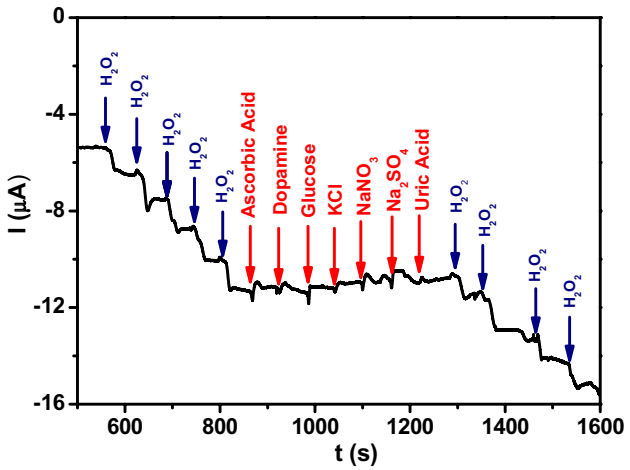

Fig. 7 Amperometric *i–t* curve obtained for Ag/TiO_2 nanocomposite (20 wt% Ag)-modified GCE for the successive addition of 50 μM of H_2O_2 and 5 mM of ascorbic acid, dopamine, glucose, KCl, $NaNO_3$, Na_2SO_4 and uric acid in 0.1 M PBS (pH7.2). Applied potential was − 0.5 V

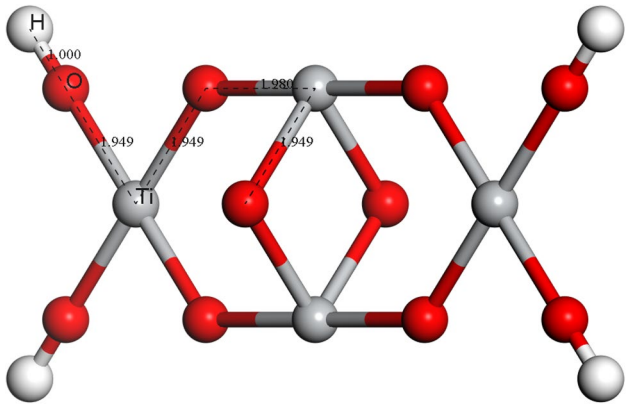

Fig. 8 Structure of $Ti_4O_{10}H_4$ cluster

For comparison, Cu_4 and Au_4 clusters are also calculated using the same procedure. Optimized geometries are shown in Figure S8. Upon adsorption on $Cu_4/Ti_4O_{10}H_4$ cluster, H_2O_2 is dissociated into H_2O and O bonded to Cu_4 cluster. The length of Cu–O bond is 1.714 Å, which compares well with the measured value of 1.72 Å for CuO [46]. The adsorption energy of H_2O_2 is calculated to be − 2.15 eV. Au_4 cluster is not stable in the presence of H_2O_2. H_2O_2 adsorbed physically to deformed Au_4 cluster with an adsorption energy of − 0.46 eV. DFT calculation supports the experimental results that TiO_2 alone has nearly no activity toward H_2O_2 reduction and the active sites are actually $Ag_4/Ti_4O_{10}H_4$ although Ag plays the key role on the absorption of H_2O_2.

4 Conclusion

In summary, a facile route to prepare Ag nanoparticles deposited on TiO_2 via a simple chemical reduction method was provided in this work. The Ag/TiO_2 nanocomposite-modified glassy carbon electrode demonstrated a better catalytic performance toward H_2O_2 reduction compared to bare TiO_2. The improvement was mainly attributed to the

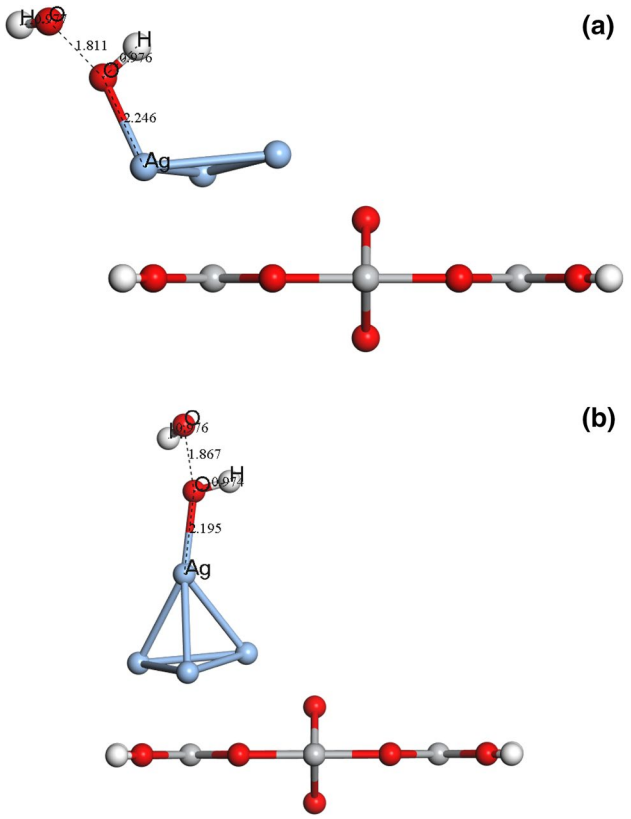

Fig. 9 Optimized geometries of $H_2O_2/Ag_3/Ti_4O_{10}H_4$ (**a**) and $H_2O_2/Ag_4/Ti_4O_{10}H_4$ (**b**), respectively

presence Ag nanoparticles which showed an excellent catalytic activity for the complete reduction of H_2O_2, while the existing TiO_2 gives Ag/TiO_2 to be a stable $Ag_4/Ti_4O_{10}H_4$. The optimum Ag content in Ag/TiO_2 for efficient sensor was found to be 20 wt%. It showed better performance with a detection limit of 1.23 µM using amperometric *i–t* curve technique. Furthermore, the nanocomposite-modified electrode showed selectivity toward the detection of H_2O_2 in the presence of a 100 times higher concentration of other analytes. This sensor was stable and selective toward the detection of H_2O_2 and it could add further credit to the TiO_2-based electrochemical sensor.

Acknowledgements This work was funded by Xiamen University Malaysia Research Fund (Grant no. XMUMRF/2018-C1/IENG/0001.

Compliance with ethical standards

Conflict of interest The authors declare no conflicts of interest.

References

1. B.E. Watt, A.T. Proudfoot, J.A. Vale, Toxicol. Rev. **23**, 51–57 (2004)
2. W. Lei, A. Dürkop, Z. Lin, M. Wu, O.S. Wolfbeis, Microchim. Acta **143**, 269–274 (2003)
3. U. Pinkernell, S. Effkemann, U. Karst, Anal. Chem. **69**, 3623–3627 (1997)
4. S. Guo, D. Wen, S. Dong, E. Wang, Talanta **77**, 1510–1517 (2009)
5. N.I. Ikhsan, P. Rameshkumar, A. Pandikumar, M.M. Shahid, N.M. Huang, S.V. Kumar, H.N. Lim, Talanta **144**, 908–914 (2015)
6. M.M. Shahid, P. Rameshkumar, A. Pandikumar, H.N. Lim, Y.H. Ng, N.M.J. Huang, Mater. Chem. A **3**, 14458–14468 (2015)
7. J.M. George, A. Antony, B. Mathew, Microchim. Acta **185**, 358 (2018)
8. C. Tortolini, P. Bollella, R. Zumpano, G. Favero, F. Mazzei, R. Antiochia, Biosensors **8**, 108 (2018)
9. Y. Cho, N.S. Parmar, S. Nahm, J.-W.J. Choi, Alloys Compd. **694**, 217–222 (2017)
10. A.L. Stroyuk, V.V. Shvalagin, S.Y. Kuchmii, J. Photochem. Photobiol. A **173**, 185–194 (2005)
11. D. Sivalingam, J.B. Gopalakrishnan, U.M. Krishnan, S. Madanagurusamy, J.B.B. Rayappan, Phys. E **43**, 1804–1808 (2011)
12. M.M. Khan, S.A. Ansari, J. Lee, M.H. Cho, Mater. Sci. Eng. C **33**, 4692–4699 (2013)
13. W. Wang, Y. Xie, C. Xia, H. Du, F. Tian, Microchim. Acta **181**, 1325–1331 (2014)
14. Y.-E. Miao, S. He, Y. Zhong, Z. Yang, W.W. Tjiu, T. Liu, Electrochim. Acta **99**, 117–123 (2013)
15. G. Mohseni, M. Negahdary, R. Malekzadeh, J. Manoochehri, A. Hadaegh, A. Sayad, H. Akbari-dastjerdi, M. Fazilati, S. Rezaei-Zarchi, Int. J. Electrochem. Sci. **7**, 7033–7044 (2012)
16. S. Yao, J. Xu, Y. Wang, X. Chen, Y. Xu, S. Hu, Anal. Chim. Acta **557**, 78–84 (2006)
17. S. Weng, Y. Zheng, C. Zhao, J. Zhou, L. Lin, Z. Zheng, X. Lin, Microchim. Acta **180**, 371–378 (2013)
18. W. Zhang, G. Xie, S. Li, L. Lu, B. Liu, Appl. Surf. Sci. **258**, 8222–8227 (2012)
19. D. Wang, L. Pang, H. Mou, Y. Zhou, C. Song, RSC Adv. **5**, 24101–24109 (2015)
20. S.P. Lim, A. Pandikumar, N.M. Huang, H.N. Lim, Int. J. Hydrog. Energy **39**, 14720–14729 (2014)
21. S.P. Lim, A. Pandikumar, N.M. Huang, H.N. Lim, G. Gu, T. Ma, RSC Adv. **4**, 48236–48244 (2014)
22. X. Chen, G. Wu, Z. Cai, M. Oyama, X. Chen, Microchim. Acta **181**, 689–705 (2014)
23. Y.-H. Won, K. Huh, L.A. Stanciu, Biosens. Bioelectron. **26**, 4514–4519 (2011)
24. M. Zheng, P. Li, C. Yang, H. Zhu, Y. Chen, Y. Tang, Y. Zhou, T. Lu, Analyst **137**, 1182–1189 (2012)
25. R. Qiu, H.G. Cha, H.B. Noh, Y.B. Shim, X.L. Zhang, R. Qiao, D. Zhang, Y. Kim, U. Pal, Y.S. Kang, J. Phys. Chem. C **113**, 15891–15896 (2009)
26. T.-H. Tsai, T.-W. Chen, S.-M. Chen, K.C. Lin, Int. J. Electrochem. Sci. **6**, 4628–4637 (2011)
27. Y. Liu, D. Wang, L. Xu, H. Hou, T. You, Biosens. Bioelectron. **26**, 4585–4590 (2011)
28. H. Zhong, R. Yuan, Y. Chai, Y. Zhang, C. Wang, F. Jia, Microchim. Acta **176**, 389–395 (2012)
29. J.-M. You, Y.N. Jeong, M.S. Ahmed, S.K. Kim, H.C. Choi, S. Jeon, Biosens. Bioelectron. **26**, 2287–2291 (2011)
30. F. Jiang, R. Yue, Y. Du, J. Xu, P. Yang, Biosens. Bioelectron. **44**, 127–131 (2013)
31. W. Lu, F. Liao, Y. Luo, G. Chang, X. Sun, Electrochim. Acta **56**, 2295–2298 (2011)
32. Q. Yi, F. Niu, L. Li, R. Du, Z. Zhou, X. Liu, J. Electroanal. Chem. **654**, 60–65 (2011)
33. Y. Han, J. Zheng, S. Dong, Electrochim. Acta **90**, 35–43 (2013)

34. S.P. Lim, A. Pandikumar, N.M. Huang, H.N. Lim, RSC Adv. **4**, 38111–38118 (2014)
35. M. Yu, J. Zhang, S. Li, Y. Meng, J. Liu, RSC Adv. **5**, 5604–5610 (2014)
36. A. Tkatchenko, M. Scheffler, Phys. Rev. Lett. **102**, 73005 (2009)
37. J.P. Perdew, K. Burke, M. Ernzerhof, Phys. Rev. Lett. **78**, 1396 (1997)
38. Z. Tian, L. Wang, L. Jia, Q. Li, Q. Song, S. Su, H. Yang, RSC Adv. **3**, 6369–6376 (2013)
39. S.P. Lim, A. Pandikumar, H.N. Lim, R. Ramaraj, N.M. Huang, Sci. Rep. **5**, 11922 (2015)
40. Y. Zhang, S. Liu, L. Wang, X. Qin, J. Tian, W. Lu, G. Chang, X. Sun, RSC Adv. **2**, 538–545 (2012)
41. X. Qin, W. Lu, Y. Luo, G. Chang, A.M. Asiri, A.O. Al-Youbi, X. Sun, Electrochim. Acta **74**, 275–279 (2012)
42. Y. Jiang, B. Zheng, J. Du, G. Liu, Y. Guo, D. Xiao, Talanta **112**, 129–135 (2013)
43. B.-H. Jeon, D.-H. Yang, Y.-D. Kim, J.S. Shin, C.-S. Lee, Electrochim. Acta **292**, 749–758 (2018)
44. H. Tada, F. Suzuki, S. Ito, T. Akita, K. Tanaka, T. Kawahara, H. Kobayashi, J. Phys. Chem. B **106**, 8714–8720 (2002)
45. K.P. Huber, G. Herzberg, (Springer, Boston, 1979)
46. M.L. Polak, M.K. Gilles, J. Ho, W.C. Lineberger, J. Phys. Chem. **95**, 3460–3463 (1991)